Journal of Industrial and Engineering Chemistry 76 (2019) 333–343

Contents lists available at ScienceDirect

Journal of Industrial and Engineering Chemistry

journal homepage: www.elsevier.com/locate/jiec

Bi-functional Al-doped ZnO@SnO_2 heteronanowires as efficient substrates for improving photocatalytic and SERS performance

Yu-Cheng Chang*, Shuo-Hsiu Wu

Department of Materials Science and Engineering, Feng Chia University, Taichung, 40724, Taiwan

ARTICLE INFO

Article history:
Received 26 January 2019
Received in revised form 15 March 2019
Accepted 30 March 2019
Available online 24 April 2019

Keywords:
Al-doped ZnO@SnO_2 heteronanowires
Surface-enhanced Raman scattering
Photocatalysts
Ag nanoparticles
Hot spots
Amoxicillin

ABSTRACT

Bi-functional Al-doped ZnO@SnO_2 heteronanowires systematically analyzed as high-performance substrates for photocatalytic and surface-enhanced Raman scattering (SERS) applications. For the photocatalytic application, the Al-doped ZnO@SnO_2 heteronanowires can exhibit highly efficient and reusable photocatalysts in the photodecomposition of rhodamine 6G solution under low-powered UV-light irradiation, which ascribed to improve the inhabitation of electron–hole pairs recombination and higher surface active sites. For the SERS application, Al-doped ZnO@SnO_2 heteronanowires revealed suitable geometry to deposit Ag nanoparticles with higher density and more hot spots in three-dimensional structures, which can provide high SERS enhancement, low detection limit (amoxicillin 10^{-10} M), high reproducibility, and stability.

Introduction

Organic dyes are one of the major organic pollutants emitted into the wastewater from industrial coatings, textiles, plastics, food, cosmetics, and consumer electronics industries [1–3]. Many of the organic dyes are toxic, non-biodegradable, and potential carcinogenicity poses a severe threat to the environment and organisms [2,4,5]. Recently, photocatalytic decomposition of organic dyes is one of the most attractive and essential technologies due to its low cost, no waste disposal problem, complete mineralization, ambient pressure, and temperature conditions [6–9]. For photocatalytic processes, metal oxides are the most commonly used photocatalysts due to the advantageous combination of electronic band structure, light absorbing properties, charge transport properties, and excited state lifetime [10–14]. Among them, ZnO is one of the most widely used as active and non-toxic metal oxide photocatalysts, which exhibits the excellences of low cost, high quantum efficiency, high photosensitivity, high redox potential, high mechanical and thermal stability [15–17]. However, there are some disadvantages in suppressing its photocatalytic abilities, such as the absorption of only UV-light, the higher recombination rate of photoinduced charge carriers, and photoinduced corrosion [18].

Several routes have adopted to improve the photocatalytic efficiency of ZnO via increasing the concentration of oxygen defects or surface active sites [19–21], doping metal ions [22,23], depositing noble metals [24–27], and coupling other semiconductors [28–32]. For ZnO coupling with other semiconductors, which can not only reduce the recombination rate of photoinduced charge carriers but also improve the light harvesting ability to enhance their photocatalytic efficiency. There are extensive reports to combine one or two kinds of semiconductor materials by coupling ZnO with metal oxide or metal sulfide, such as TiO_2 [33], ZnS [34], SnO_2 [35], Bi_2S_3 [36], or In_2S_3 [37] by virtue of their highly efficient photocatalytic performance and remarkable recycling stability. Among these semiconductor materials, SnO_2 is an n-type wide direct bandgap (3.49 eV at room temperature) semiconductor with unique physical and chemical properties, which has widely used in lithium-ion batteries [38], supercapacitors [39], gas sensors [40], photovoltaic cells [41], and photocatalysts [42]. Recently, ZnO/SnO_2 heterostructures have attracted considerable interests due to their particular bandgap position, which can restain the recombination of photoinduced charge carriers and improve the photocatalytic activity [43,44]. Also, ZnO/SnO_2 heterostructures with nanopowder form can provide ultrahigh surface active sites to enhance the photocatalytic degradation of organic dyes [45,46]. However, some problems need to overcome during photocatalytic reuse, such as aggregation, poor durability, and recyclability [47]. Given that ZnO/SnO_2 heterostructures directly grow on the substrates, which may supply a suitable way to improve these problems [48].

* Corresponding author.
E-mail address: yuchchang@fcu.edu.tw (Y.-C. Chang).

https://doi.org/10.1016/j.jiec.2019.03.058
1226-086X/

Surface-enhanced Raman scattering (SERS) has demonstrated as a versatile analytical technique that further enhanced Raman intensity via adsorbing the number of molecules on the surface of nanostructured metals [49–51]. Up to now, SERS technology has recognized as one of the most sensitive and promising analytical tools in the chemical, biological, environmental and clinical fields due to it provided a wealth of structural information in a non-destructive manner [52]. In most cases, two primary mechanisms have been employed to explain the SERS enhancement effect. One is an electromagnetic mechanism, which excitation occurs in local surface plasmon resonance (LSPR) on the surface of the noble metal and the electric field is amplified in an enhancement factor (EF) of 10^6 [53]. The other is the chemical mechanism. It belongs to the charge transfer between the target molecule and the surface of the substrate, which can significantly amplify the molecular polarization tensor and improve Raman enhancement [54,55]. For electromagnetic mechanisms, SERS substrates with noble metal nanostructures can effectively adjust by controlling their size, shape, and distribution on suitable support materials [56,57]. However, some problems limit the development of SERS substrates, such as low nanostructure density, uncontrolled aggregation, and uneven distribution of nanostructures [55,58]. Recently, one-dimensional ZnO nanostructures with decorated noble metal nanoparticles have been shown to provide good SERS substrates due to their excellent detection sensitivity, stability, uniformity, and biocompatibility [59,60]. Compared to binary heterostructures (ZnO/noble metal nanoparticles), ternary heterostructures with well-controlled hierarchical morphology (ZnO and semiconducting/noble metal nanoparticles) have attracted considerable attention [61].

In this article, Al-doped ZnO@SnO_2 heteronanowires have synthesized via a facile wet chemical and hydrothermal methods for enhanced photocatalytic and SERS performance. The concentration of SnO_2 precursor can control the shell thicknesses of SnO_2. The morphology, crystal structure, chemical composition, growth mechanism, optical absorption and emission properties of the Al-doped ZnO@SnO_2 heteronanowires demonstrated by using various microscopic and spectroscopic methods. Al-doped ZnO@SnO_2 heteronanowires can improve photoelectron–hole pair separation and more surface active sites for enhancing their photocatalytic efficiency and reusability. Also, Al-doped ZnO@SnO_2 heteronanowires provided better geometry for the deposition of uniform-sized Ag nanoparticles, which facilitated the fabrication of high-performance SERS substrate for multiple detections of different molecular species.

Experimental

Chemical and reagents

Acetone (CH_3COCH_3, 99.9%, Sigma-Aldrich), ethanol (C_2H_5OH, 99.8%, Sigma-Aldrich), zinc acetate dihydrate ($Zn(CH_3COO)_2{\cdot}2H_2O$, 98%, Sigma-Aldrich), zinc nitrate hexahydrate ($Zn(NO_3)_2{\cdot}6H_2O$, 98%, Sigma-Aldrich), hexamethylenetetramine (HMTA, $(CH_2)_6N_4$, 99%, Sigma-Aldrich), 1,3 diaminopropane (DAP, $NH_2(CH_2)_3NH_2$, 99%, Sigma-Aldrich), aluminum sulfate hydrate ($Al_2(SO_4)_3{\cdot}18H_2O$, 97%, Sigma-Aldrich), sodium stannate trihydrate ($Na_2SnO_3{\cdot}3H_2O$, 98%, Alfa Aesar), urea (NH_2CONH_2, 99%, J. T. Baker), rhodamine 6G (R6G, $C_{28}H_{31}N_2O_3Cl$, 99%, Sigma-Aldrich), zinc oxide nanopowder (ZnO nanopowder, 99%, 7–13 nm, Alfa Aesar), titanium(IV) oxide nanopowder (TiO_2 nanopowder, 99.7%, 15 nm, Alfa Aesar), aluminum oxide nanopowder (Al_2O_3 nanopowder, 99.5%, 40–50 nm, Alfa Aesar), para-benzoquinone (p-BQ, 98%, Sigma-Aldrich), isopropyl alcohol (IPA, 99.5%, Alfa Aesar), and amoxicillin ($C_{16}H_{19}N_3O_5S$, 100 mg/mL, Alfa Aesar) were used without further purification. DI water with the resistivity greater than 18.2 MΩ was used for all solution preparations.

Fabrication of Al-doped ZnO nanowires

In this article, Al-doped ZnO@SnO_2 heteronanowires have been synthesized via a facile wet chemical and hydrothermal methods for enhanced photocatalytic and SERS performance. Glass substrate sequentially immersed in ultrasonic baths of acetone, DI water, and ethanol for 15 min, respectively. The ZnO seed film was grown on the glass substrate by spin coating (2-min holding time, 1-min spin coating, and spin rate: 2000 rpm) a layer of the solution of 20 mM zinc acetate dihydrate in ethanol and then heated at 350 °C for 20 min under ambient condition [59,62]. The fabrication of Al-doped ZnO nanowires on the glass substrate with ZnO seed film was via a wet chemical approach in an aqueous solution (100 mL) containing 10 mM zinc nitrate hexahydrate, 10 mM HMTA, 0.13 M DAP, and 2 mM aluminum sulfate hydrate at 85 °C for 3 h. The substrate was washed with DI water and ethanol, respectively. Finally, the substrate dried at 80 °C for 2 h under ambient condition.

Fabrication of Al-doped ZnO@SnO_2 heteronanowires

Al-doped ZnO@SnO_2 heteronanowires fabricated on the Al-doped ZnO nanowires via a simple hydrothermal method in an aqueous solution (50 mL) containing the different concentration of tin dioxide (SnO_2) reaction precursor (the concentration ratio of sodium stannate trihydrate and urea is 1:40) at 120 °C for 1 h [48]. The substrate was washed with DI water and ethanol, respectively. Finally, the substrate dried at 80 °C for 2 h under ambient condition. The experimental conditions listed in Table S1 (in the Supplementary data).

Characterization

Field-emission scanning electron microscopy (FESEM) performed with a Hitachi S-4800 at an accelerating voltage of 10 kV. X-ray diffraction patterns of the samples collected by using a Bruker D2 phaser with CuKα radiation (λ = 0.154 nm). Field-emission transmission electron microscopy (FETEM) performed with a JEM-2100F at an accelerating voltage of 200 kV. The bonding characteristics of the as-fabricated samples recorded from X-ray photoelectron spectroscopy (XPS) by using a ULVAC-PHI PHI 5000 Versaprobe II system. The micro-photoluminescence (m-PL) measurement was carried out by using a He–Cd laser with an emission wavelength of 325 nm as the excitation source at the room temperature. The UV–vis diffuse reflection spectra were obtained by using UV–vis spectroscopy (Hitachi U-2900 UV/vis spectroscopy). Raman spectra were obtained in back-scattering configuration at room temperature by using a confocal Raman microscope (MRI532S, Protrustech, Taiwan). The light source was a He–Ne laser with an emission wavelength of 532 nm.

Photocatalytic measurement

The photocatalytic efficiency of as-fabricated samples on the glass substrates (1.5 × 2.5 cm^2), SnO_2 nanostructures (24 mM SnO_2 precursor), commercial ZnO nanopowder, TiO_2 nanopowder, and Al_2O_3 nanopowder were estimated by the photodegradation of an aqueous solution of R6G (0.021 mM) under a 10 W (Philip, λ_{max} = 254 nm) UV-light irradiation [63]. The powder-type of photocatalysts (such as SnO_2 nanostructures (24 mM SnO_2 precursor), commercial ZnO nanopowder, TiO_2 nanopowder, and Al_2O_3 nanopowder) were dispersed in an R6G solution (15 mg L^{-1}). The concentration of the R6G solution determined via a Hitachi U-2900 UV/vis spectroscopy at the characteristic absorption (λ_{max} = 526 nm) of R6G. The photocatalytic efficiency of as-fabricated samples on the glass substrates, SnO_2 nanostructures (24 mM SnO_2

precursor), commercial ZnO nanopowder, TiO_2 nanopowder, and Al_2O_3 nanopowder under UV-light irradiation defined as C/C_0, C_0 and C were the initial and instantaneous concentrations of R6G solution, respectively. In order to detect the superoxide radical anions ($O_2^{\bullet-}$) and hydroxyl groups ($OH^{\bullet}$) species during the photocatalytic reaction, p-BQ (10 mM) and IPA (2 mL) were added to an R6G solution dispersed with the photocatalysts to capture $O_2^{\bullet-}$ and $OH^{\bullet}$, respectively.

SERS measurement

For SERS substrates, the Ag nanoparticles deposited on the Al-doped ZnO nanowires and Al-doped ZnO@SnO_2 heteronanowires at room temperature by sputtering a silver target (99.99%, Summit-Tech Company) with an ion-beam sputtering system at a pressure of $\sim 5 \times 10^{-6}$ Torr in an ambient of Ar for 3 min. For analytes, the different concentrations of R6G and amoxicillin solution prepared by the mixed solvent of ethanol and water (volume ratio = 1:1) [64]. SERS substrates immersed into the solution at the room temperature for 1 h in the dark and dried with an air purge. For Raman measurement, the irradiation power of the laser was set at 1% 100 mW, while the integration adjusted to 1 s.

Results and discussion

Preparation and characterization of Al-doped ZnO@SnO_2 heteronanowires

Fig. 1a illustrates the procedure used to fabricate Al-doped ZnO@SnO_2 heteronanowires on the glass substrate. The fabrication processes can be briefly divided into two steps: (1) growth of Al-doped ZnO nanowires by a facile wet chemical method on the glass substrate and (2) growth of SnO_2 nanostructures onto the Al-doped ZnO nanowires. Fig. 1b shows the 45° tilt-view FESEM image described Al-doped ZnO nanowires have been fabricated on the glass substrate at 85 °C for 3 h via a wet chemical method. The cross-sectional FESEM image of Al-doped ZnO nanowires was vertically-aligned on the glass substrate (Fig. S1). The average size and length of Al-doped ZnO nanowires were 87.6 ± 16.1 nm and 5.5–6.2 μm, respectively. Fig. 1c–g show the FESEM images described the Al-doped ZnO@SnO_2 heteronanowires have been synthesized at the different concentrations of SnO_2 reaction precursor (the concentration ratio of sodium stannate trihydrate and urea is 1:40) by a hydrothermal method at 120 °C for 1 h. The concentrations of SnO_2 reaction precursor were 3, 6, 12, 24, and 48 mM, respectively. The average sizes of Al-doped ZnO@SnO_2 heteronanowires were 104.7 ± 21.3, 123.4 ± 24.1, 156.3 ± 43.1, 203.7 ± 66.7, and 356.6 ± 97.6 nm, respectively. As the concentration of the SnO_2 reaction precursor increased, the dimensions of Al-doped ZnO@SnO_2 heteronanowires gradually increased. In addition, the increased in the dimensions of the Al-doped ZnO@SnO_2 heteronanowires can also prove that the shell thicknesses of SnO_2 steadily increased with the concentration of SnO_2 reaction precursor. Also, Al-doped ZnO@SnO_2 heteronanowires grown with a high concentration of SnO_2 reaction precursor (48 mM) were more easily to aggregate with each other. The dimensions of Al-doped ZnO@SnO_2 heteronanowires can appropriately control by the concentration of SnO_2 reaction precursor.

The ex-situ observation shall be provided direct evidence to understand the growth mechanism of Al-doped ZnO@SnO_2 heteronanowires in the growth process. Fig. S2 shows the 45° tilt-view FESEM images of Al-doped ZnO@SnO_2 heteronanowires were fabricated from 24 mM SnO_2 reaction precursor at the different reaction time of 15, 30, 45, and 60 min, respectively. At the beginning of the reaction (Fig. S2a and b), SnO_2 nanocrystals decorated onto the side of Al-doped ZnO nanowires. As the

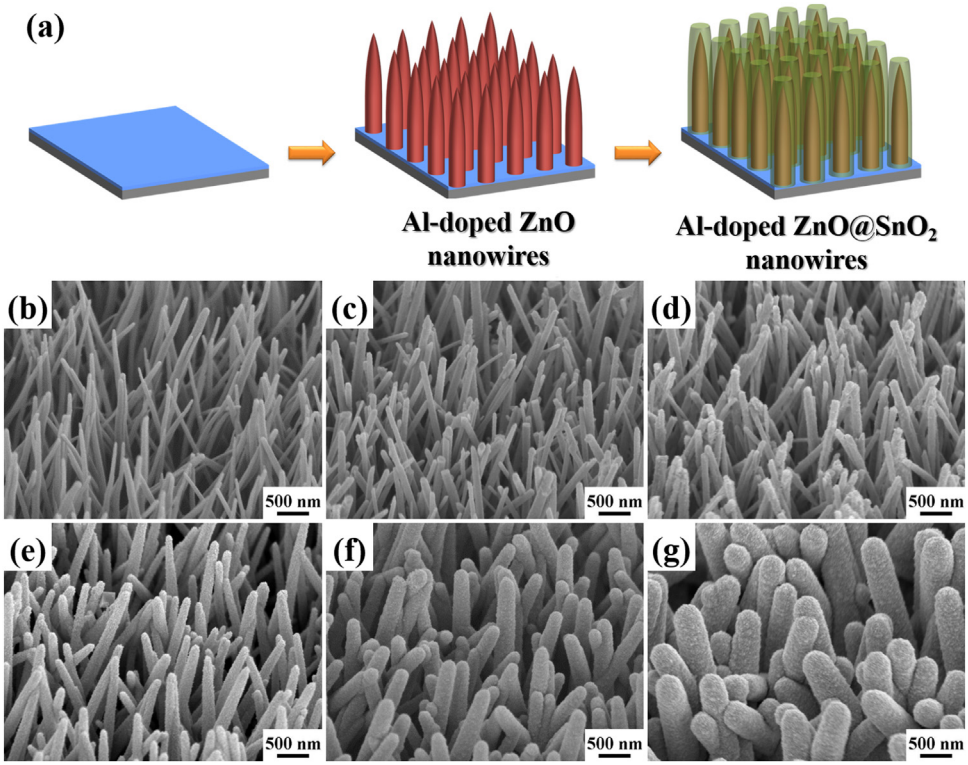

Fig. 1. (a) Schematic diagram describes the preparation of Al-doped ZnO@SnO_2 heteronanowires. The 45° tilt-view FESEM images of (b) Al-doped ZnO nanowires and (c–g) different sizes of Al-doped ZnO@SnO_2 heteronanowires fabricated on the glass substrates with ZnO seed film and Al-doped ZnO nanowires at the different concentrations of SnO_2 reaction precursor, respectively. The different concentrations of SnO_2 reaction precursor were (c) 3, (d) 6, (e) 12, (f) 24, and (g) 48 mM, respectively.

reaction time increased (Fig. S2c and d), the side and top of the Al-doped ZnO nanowires were wholly decorated with SnO_2 nanoparticles. Based on the SEM results, the appropriate reaction time can be beneficial to grow Al-doped ZnO@SnO_2 heteronanowires on the glass substrate.

The XRD pattern (Fig. 2a) of Al-doped ZnO nanowires was fabricated on the glass substrate. The diffraction peaks appeared at $2\theta = 34.5°$, 62.9°, and 72.7°, which assigned to (002), (103), and (004) crystal phases of hexagonal ZnO (JCPDS Card No. 05-0664). The diffraction peak at [002] of the Al-doped ZnO nanowires (Fig. S3) exhibited an apparent shift to the low angle as compared with pure ZnO nanowires, which reflected the lattice distortion due to the substitution of Al^{3+} for Zn^{2+} [65]. The XRD pattern (Fig. 2b) of Al-doped ZnO@SnO_2 heteronanowires was fabricated from the concentration of SnO_2 reaction precursor of 24 mM by hydrothermal method at 120 °C for 1 h. There were four new peaks displayed at 26.6°, 33.9°, 37.9°, and 51.8°, corresponding to (110), (101), (200), and (211) crystal planes of tetragonal SnO_2 (JCPDS Card No. 88-0287). There was no remarkable shift in the diffraction peaks, and other crystalline impurities no observed. This result can prove that products consist of ZnO and SnO_2. XPS further analyzed the composition and chemical states of the elements in Al-doped ZnO@SnO_2 heteronanowires. The X-ray photoelectron survey spectrum (Fig. 3a) of the Al-doped ZnO@SnO_2 heteronanowires revealed that the sample consisted of Zn, Al, Sn, and O. The high-resolution XPS spectra of Al 2p and Sn 3d for Al-doped ZnO@SnO_2 heteronanowires obtained in Fig. 3b and c, respectively. For Al 2p XPS spectrum, this binding energy consisted with the previous works (Al 2p: 73.8 eV) of oxidation state closed to +3 as well as lower than the pure Al_2O_3 (Al 2p: 75.6 eV) and above metallic Al (Al 2p: 72.8 eV), which confirmed the presence and the state change of Al in the doped ZnO system [66,67]. For Sn 3d XPS spectrum, the Sn 3d peaks revealed symmetric signals, which was attributed to the Sn $3d_{5/2}$ (486.4 eV) and Sn $3d_{3/2}$ (494.8 eV) binding energies of Sn (IV) [68]. This result can prove the composition of Al-doped ZnO@SnO_2 heteronanowires.

Detailed microstructures and compositions of the Al-doped ZnO@SnO_2 heteronanowire further investigated by FETEM. A FETEM image of a single Al-doped ZnO@SnO_2 heteronanowire, as shown in Fig. 4a. It can observe that SnO_2 nanoparticles have been wholly decorated on the Al-doped ZnO nanowire to form Al-doped ZnO@SnO_2 heteronanowire. Fig. 4b shows the SAED pattern of Al-doped ZnO@SnO_2 heteronanowire, which contributed to single-crystalline Al-doped ZnO nanowire and polycrystalline SnO_2 nanoparticles. For Al-doped ZnO nanowire, it displayed a (-110)

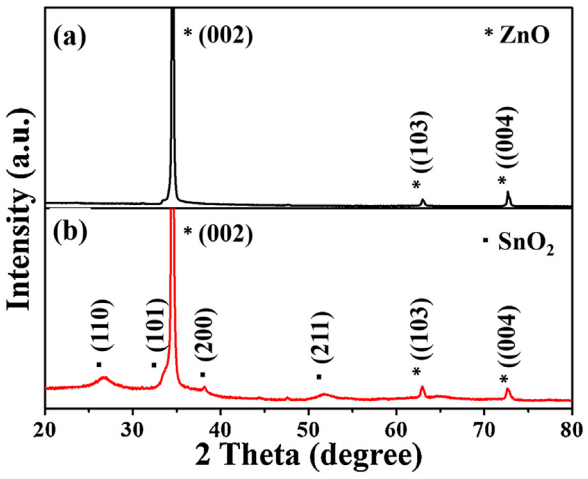

Fig. 2. XRD spectra of (a) Al-doped ZnO nanowires and (b) Al-doped ZnO@SnO_2 heteronanowires (24 mM SnO_2 precursor) fabricated on the glass substrates.

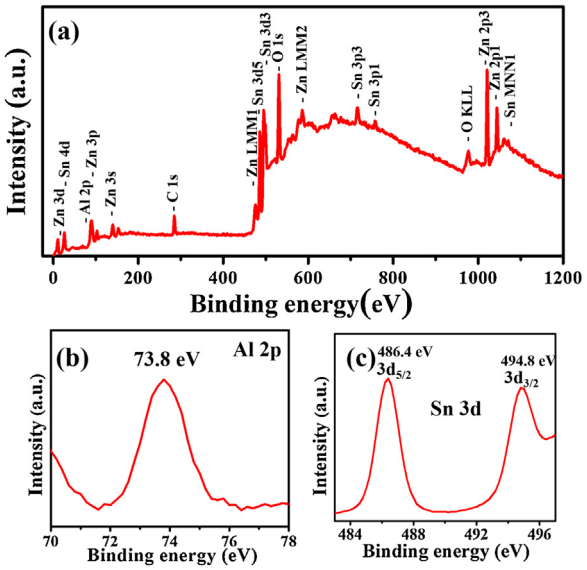

Fig. 3. (a) The XPS survey spectrum of Al-doped ZnO@SnO_2 heteronanowires (24 mM SnO_2 precursor) fabricated on the glass substrate in Fig. 1f. The XPS (b) Al 2p and (c) Sn 3d spectra of Al-doped ZnO@SnO_2 heteronanowires (24 mM SnO_2 precursor) fabricated on the glass substrate.

zone-axis SAED pattern of hexagonal ZnO (JCPDS No. 89-1397). For SnO_2 nanoparticles, it presented a concentric ring can assign as diffraction from [101] plane of tetragonal structured SnO_2 (JCPDS Card No. 88-0287). The HRTEM image (Fig. 4c) was taken from a portion of Al-doped ZnO@SnO_2 heteronanowire. Fig. 4d illustrated the HRTEM image of Al-doped ZnO nanowire (Fig. 4c region A). The interlayer spacing of the region of Al-doped ZnO nanowire obtained 0.260 nm, which was accordant with the *d*-spacing of the [002] lattice plane of the hexagonal ZnO crystal. The HRTEM image (Fig. 4e) of SnO_2 nanoparticles (Fig. 4c region B) exhibited the interlayer spacing of 0.264 nm, which was accordant with the *d*-spacing of the [101] lattice plane of the tetragonal SnO_2 crystal [42]. According to the low magnification of HAADF-TEM image (Fig. 4f) revealed SnO_2 nanoparticles, which have been completely covered on the Al-doped ZnO nanowire. Furthermore, the EDS mapping analysis of an Al-doped ZnO@SnO_2 heteronanowire also confirmed the heterostructured construction of Al-doped ZnO nanowire core and SnO_2 nanoparticles sheath, in which the signal distributions of Zn, O, Al, and Sn exhibited similar shapes, as shown in Fig. 4g–j. The contents of Zn, O, Al, and Sn elements were obtained about 39.6, 56.4, 0.7, and 3.3 atomic %, respectively. This result indicated that an Al-doped ZnO@SnO_2 heteronanowire has successfully fabricated in the reaction process. The SEM and XRD results can also support this result.

Optical properties of Al-doped ZnO@SnO_2 heteronanowires

The emission properties of the Al-doped ZnO nanowires and Al-doped ZnO@SnO_2 heteronanowires investigated at room temperature in an m-PL device. The PL spectra (Fig. 5a) of Al-doped ZnO nanowires and Al-doped ZnO@SnO_2 heteronanowires (24 mM SnO_2 precursor) fabricated on the glass substrates. For Al-doped ZnO nanowires, the weak UV emission at 379 nm (3.27 eV) was related to the band gap of ZnO. For Al-doped ZnO@SnO_2 heteronanowires, the UV emission at 383 nm (3.24 eV) in the 363–455 nm wavelength range was very stronger and broader, which ascribed to the inherent defect structure of SnO_2 during the growth process, such as oxygen vacancies [42,69,70]. Fig. 5b shows the UV–vis diffuse reflection spectra of Al-doped ZnO nanowires and Al-doped ZnO@SnO_2 heteronanowires (24 mM SnO_2

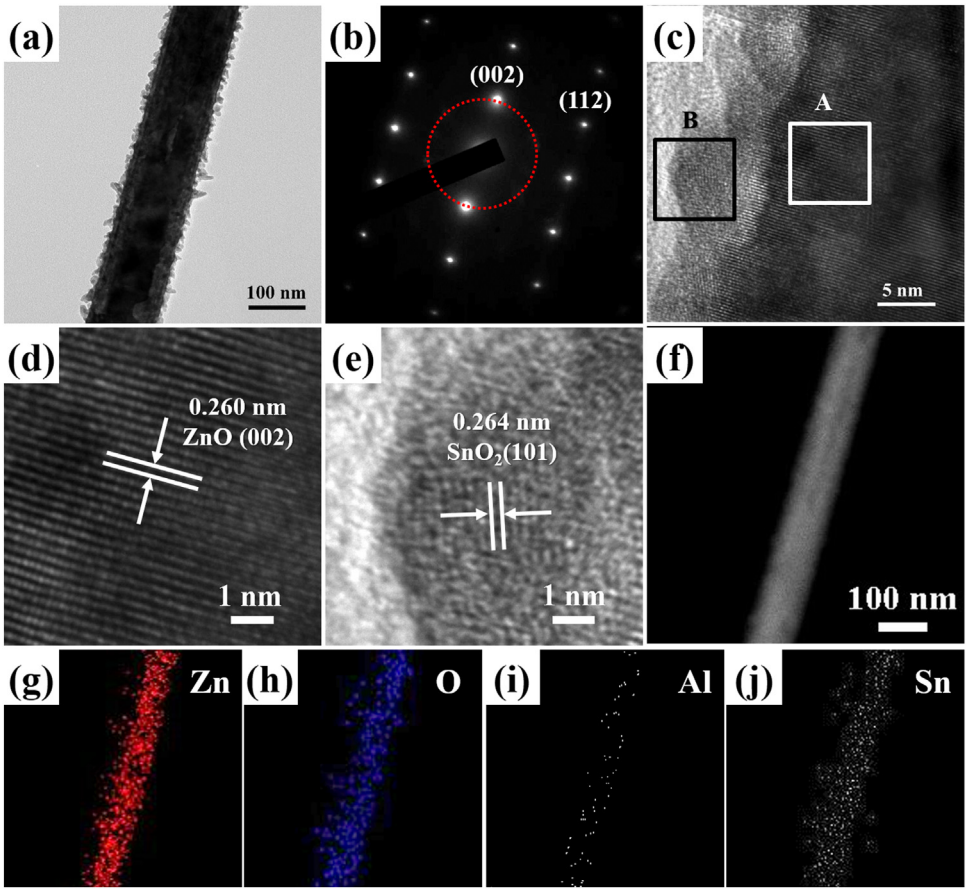

Fig. 4. (a) TEM, (b) SAED pattern, (c–e) HRTEM, (f) HAADF, and (g–j) EDS mapping images of an Al-doped ZnO@SnO_2 heteronanowire (24 mM SnO_2 precursor) fabricated on the glass substrate in Fig. 1f. The EDS mapping images were (g) Zn, (h) O, (i) Al, and (j) Sn, respectively.

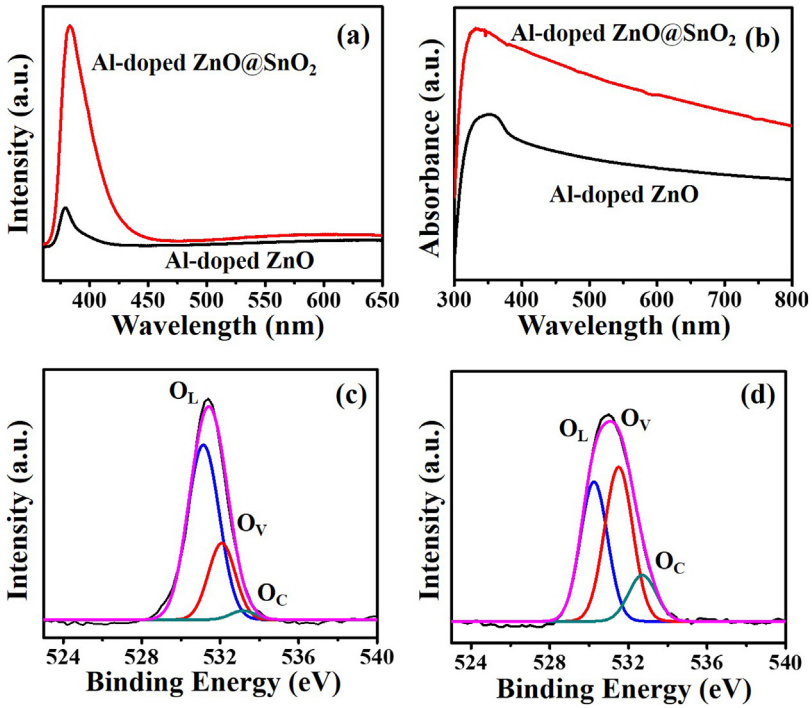

Fig. 5. (a) PL spectra and (b) UV–vis absorption spectra of Al-doped ZnO nanowires and Al-doped ZnO@SnO_2 heteronanowires (24 mM SnO_2 precursor) fabricated on the glass substrates, respectively. The XPS O1s spectra of (c) Al-doped ZnO nanowires and (d) Al-doped ZnO@SnO_2 heteronanowires (24 mM SnO_2 precursor) fabricated on the glass substrates.

precursor). It observed that the Al-doped ZnO@SnO_2 heteronanowires revealed stronger absorption from UV-light to visible-light in the range of 300–800 nm compared to Al-doped ZnO nanowires. In order to understand the oxygen vacancies in Al-doped ZnO nanowires and Al-doped ZnO@SnO_2 heteronanowires (24 mM SnO_2 precursor), the chemical states of O 1s were measured by XPS, as shown in Fig. 5c and d. The binding energy peaks of 530.2, 531.5, and 532.7 eV observed in Al-doped ZnO nanowires and Al-doped ZnO@SnO_2 heteronanowires, which associated with lattice oxygen (O_L), oxygen vacancies (O_V) or defects, and chemisorbed oxygen (O_C), respectively [37,43,69]. For the relative intensity of O_V (531.7 eV) peak, Al-doped ZnO@SnO_2 heteronanowires were higher than Al-doped ZnO nanowires, which revealed that Al-doped ZnO@SnO_2 heteronanowires have a higher amount of oxygen vacancies. The oxygen vacancies acted the positive charge centers to trap electrons, which can enhance the photocatalytic activity of Al-doped ZnO@SnO_2 heteronanowires by separating the electron–hole pairs. The appropriate amount of oxygen vacancies and stronger absorption properties of Al-doped ZnO@SnO_2 heteronanowires can provide an effective method to promote the photocatalytic performance.

Photocatalytic performances of Al-doped ZnO@SnO_2 heteronanowires

The photocatalytic efficiency of Al-doped ZnO nanowires and Al-doped ZnO@SnO_2 heteronanowires with different concentration of SnO_2 reaction precursor comparatively investigated by the decomposition of an organic dye (R6G) solution under low-powered UV-light irradiation, as shown in Fig. 6a. The photocatalytic efficiency of Al-doped ZnO nanowires and Al-doped ZnO@SnO_2 heteronanowires with different concentrations of SnO_2 reaction precursor were 58.8 (0 mM), 97.7 (3 mM), 99.1 (6 mM), 99.2 (12 mM), 99.5 (24 mM), and 99.2% (48 mM), respectively. Compared with Al-doped ZnO nanowires, the different sizes of Al-doped ZnO@SnO_2 heteronanowires exhibited to enhance photocatalytic activity in the photodegradation of R6G in aqueous solution. Langmuir–Hinshelwood model has been widely adopted to evaluate the photodegradation kinetics of organic dyes in the aqueous solution [71]. The reaction-rate constants (k) of Al-doped ZnO@SnO_2 heteronanowires with different concentrations of SnO_2 precursor were 0.0051 (0 mM), 0.0227 (3 mM), 0.0269 (6 mM), 0.0290 (12 mM), 0.0321 (24 mM), and 0.0273 min^{-1} (48 mM), respectively, as shown in Fig. 6b. The Al-doped ZnO@SnO_2 heteronanowires (24 mM SnO_2 precursor) revealed the highest photocatalytic activity in the decomposition of the R6G solution. When the concentration of the SnO_2 precursor was less than 24 mM, the photocatalytic efficiency increased as the concentration of the SnO_2 precursor increased. However, the concentration of the SnO_2 precursor further increased to more than 24 mM; it exhibited the opposite tendency. This phenomenon attributed the bound together of Al-doped ZnO@SnO_2 heteronanowires to decrease the surface active sites of photocatalysts. Compared to Al-doped ZnO nanowires, Al-doped ZnO@SnO_2 heteronanowires (24 mM SnO_2 precursor) exhibited about 6.3 times reaction-rate constant (k). The possible reasons ascribed the coupling effects of Al-doped ZnO nanowires and SnO_2 shells to reduce photoinduced electron–hole pair recombination and provide higher surface active sites for enhancing the photocatalytic efficiency.

The photocurrent response experiments can be used to demonstrate the coupling effects of Al-doped ZnO nanowires and SnO_2 shells. Al-doped ZnO@SnO_2 heteronanowires (24 mM SnO_2 precursor) can provide a stronger photoresponse than Al-

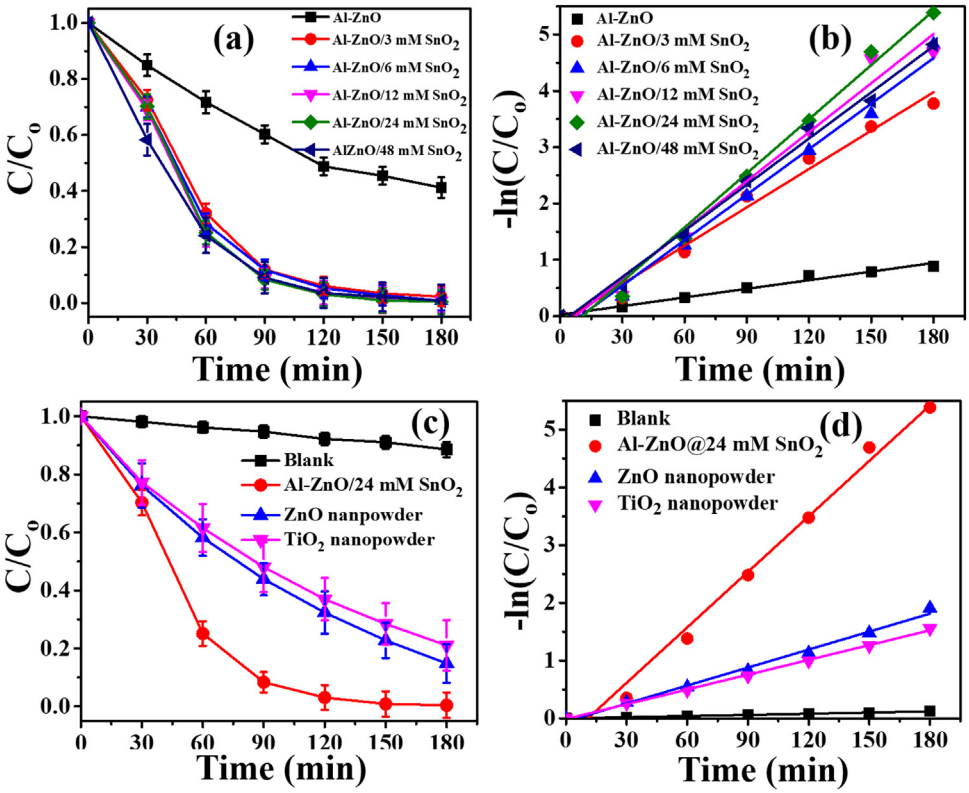

Fig. 6. (a) The photocatalytic activities of Al-doped ZnO nanowires and Al-doped ZnO@SnO_2 heteronanowires of different sizes fabricated on the glass substrates as photocatalysts for the degradation of the R6G solution under UV-light irradiation. (b) Kinetic simulation curves of R6G degradation over (a). (c) The photocatalytic activities of blank (without photocatalysts), Al-doped ZnO@SnO_2 heteronanowires (24 mM SnO_2 precursor) fabricated on the glass substrate, ZnO nanopowder, and TiO_2 nanopowder as photocatalysts for the degradation of the R6G solution. (d) Kinetic simulation curves of R6G degradation over (c).

doped ZnO nanowires under UV-light irradiation (Fig. S4). Due to Al-doped ZnO@SnO_2 heteronanowires can enhance charge carrier separation and migration for raising their photocatalytic activity. Also, the doping of Al can also play a critical role to increase the photocatalytic efficiency of ZnO@SnO_2 heteronanowires. From Fig. S5, the Al-doped ZnO nanowires exhibited the similar PL emission peaks of ZnO nanowires, the intensity of all emission peaks decreased. It established that Al-doped ZnO nanowires can effectively hinder the photoinduced electron–hole pair recombination. The ZnO@SnO_2 heteronanowires (24 mM SnO_2 precursor) fabricated on the glass substrates and powder-type of SnO_2 nanostructures (24 mM SnO_2 precursor) can use to evaluate the photocatalytic efficiency (Fig. S6). Compared to ZnO@SnO_2 heteronanowires and SnO_2 nanostructures, Al-doped ZnO@SnO_2 heteronanowires can enhance the efficient separation of photoinduced electron–hole pairs by Al-doped ZnO and provide a higher surface active sites by against aggregation for improving the photodecomposition of R6G solution.

Fig. 6c shows the photocatalytic activity of blank (without photocatalysts), Al-doped ZnO@SnO_2 heteronanowires (24 mM SnO_2 precursor) grown on a glass substrate, commercial ZnO nanopowder (7–13 nm) and TiO_2 nanopowder (15 nm). The photocatalytic efficiency of blank, Al-doped ZnO@SnO_2 heteronanowires (24 mM SnO_2 precursor), commercial ZnO nanopowder and TiO_2 nanopowder were 11.4, 99.5, 85.1, and 78.9%, respectively. Al-doped ZnO@SnO_2 heteronanowires (24 mM SnO_2 precursor) also exhibited more excellent photocatalytic degradation of the R6G solution rather than that of commercial ZnO nanopowder (7–13 nm) and TiO_2 nanopowder (15 nm). Also, the degree of mineralization of R6 G solution with Al-doped ZnO@SnO_2 heteronanowires was estimated by the determination of the decrease in the total organic carbon (TOC) for the reaction solution, as shown in Fig. S7. It can be seen that the TOC has gradually decreased with irradiation time. The reaction-rate constants (k) of different materials (Fig. 6d) were 0.0007 (blank), 0.0321 (Al-doped ZnO@SnO_2 heteronanowires), 0.0104 (ZnO), and 0.0085 min^{-1} (TiO_2), respectively. The results revealed that Al-doped ZnO@SnO_2 heteronanowires were about 3.1 and 3.8 times greater than commercial ZnO and TiO_2 nanopowder, respectively. This result may attribute to Al-doped ZnO@SnO_2 heteronanowires directly fabricated on the glass substrate, which can provide more surface active sites to prevent aggregation rather than commercial ZnO and TiO_2 nanopowder. In addition, Al-doped ZnO@SnO_2 heteronanowires can also exhibit high photocatalytic activity in the decomposition of the colorless organic pollutant (such as 4-nitrophenol), as shown in Fig. S8.

The reusability of photocatalysts was also an essential issue as their efficiency in the photocatalytic process. The glass substrate with fabricated Al-doped ZnO@SnO_2 heteronanowires (24 mM) was immersed in the R6G solution and irradiated with UV-light for 3 h; the substrate was washed with DI water to remove the residual R6G solution and dried under an air purge. This substrate immersed in the same concentration of R6G solution for the next photodecomposition cycle. For the five cycles, the photocatalytic efficiency (Fig. 7) of the Al-doped ZnO@SnO_2 heteronanowires fabricated with 24 mM SnO_2 reaction precursor on a glass substrate were 99.1, 98.6, 99.4, 99.5, and 99.0% respectively. The results revealed Al-doped ZnO@SnO_2 heteronanowires on a glass substrate with higher eusability for the decomposition of the R6G solution. The FESEM image (Fig. S9) and XPS spectrum (Fig. S10) measured the recycled Al-doped ZnO@SnO_2 heteronanowires, which were almost similar to the fresh photocatalysts (Figs. 1f and 3 a), respectively. Furthermore, Al-doped ZnO@SnO_2 heteronanowires directly grown on a glass substrate simplified the recycling process, resulting in a highly stable and cost-effective photocatalyst.

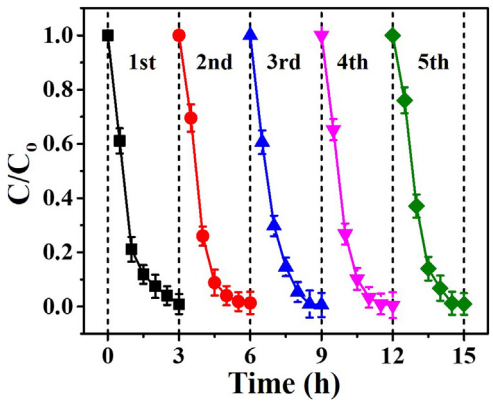

Fig. 7. The reusability test of the Al-doped ZnO@SnO_2 heteronanowires (24 mM SnO_2 precursor) fabricated on the glass substrate for the photodegradation of R6G solution under UV-light irradiation.

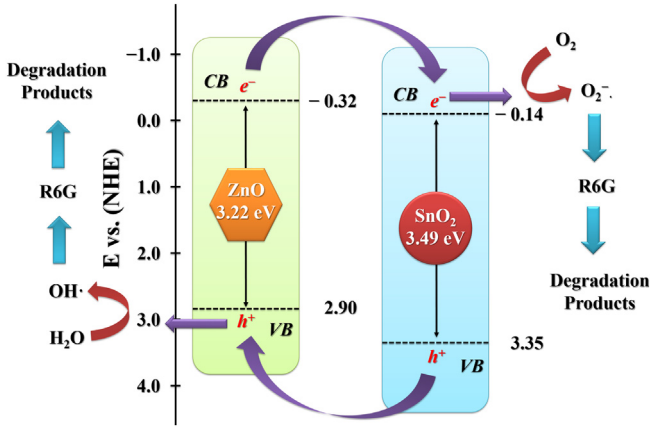

Fig. 8. Schematic diagram for the photocatalytic mechanism of Al-doped ZnO@SnO_2 heteronanowires under UV-light irradiation.

The possible mechanism of R6G photodegradation in the present of Al-doped ZnO@SnO_2 heteronanowires proposed in Fig. 8. For SnO_2, the edge potential of the valence band (VB) and conduction band (CB) were 3.35 and −0.14 eV (vs. the normal hydrogen electrode (NHE)), respectively [72]. For ZnO, the edge potential of VB and CB were 2.9 and −0.32 eV (vs. NHE), respectively [37]. The photoinduced electrons in the CB of SnO_2 nanoparticles could migrate into the CB of Al-doped ZnO nanowires. Also, the photogenerated holes in the VB of Al-doped ZnO nanowires could migrate into the VB of SnO_2 nanoparticles. This phenomenon ascribed to the efficient spatial separation of electrons and holes. The photoinduced electrons on the CB of Al-doped ZnO nanowires could react with O_2 molecules via dissolved oxygen to generate superoxide radical anions ($O_2^{\bullet}$−) [22]. Also, the photoinduced holes on the VB of SnO_2 nanoparticles could react with H_2O molecules via dissolved water to break them into hydroxyl groups ($OH^{\bullet}$). In order to clarify the contribution of active species of $O_2^{\bullet}$− and $OH^{\bullet}$ in the photocatalytic reaction of Al-doped ZnO@SnO_2 heteronanowires. Herein, para-benzoquinone (p-BQ) and isopropyl alcohol (IPA) were selected as radical scavengers to trap photogenerated $O_2^{\bullet}$− and $OH^{\bullet}$ species, respectively [73,74]. The influence of p-BQ and IPA on the photocatalytic reaction were shown in Fig. S11. It can exhibit the photocatalytic degradation of R6G decreased significantly with the addition of p-BQ and IPA. This result can demonstrate that the $O_2^{\bullet}$− and $OH^{\bullet}$ species were the dominant active species in the photocatalytic reaction of Al-doped ZnO@SnO_2 heteronanowires.

SERS performances of Al-doped ZnO@SnO_2 heteronanowires

Al-doped ZnO@SnO_2 heteronanowire has proper geometry, which can facilitate to deposit the uniform sizes of Ag nanoparticles. Herein, we used an ion sputtering system to deposit Ag nanoparticles on the surface of Al-doped ZnO nanowires and Al-doped ZnO@SnO_2 heteronanowires with different concentration of SnO_2 reaction precursor at room temperature for 3 min. Fig. 9 represents backscatter electron (BSE) images of Al-doped ZnO nanowires and different sizes of Al-doped ZnO@SnO_2 heteronanowires with decorated Ag nanoparticles. The amount of backscattered electrons was highly dependent on the atomic number of the sample. Due to Ag has a higher atomic number than zinc and oxygen, Ag nanoparticles can exhibit the brighter than ZnO in the BSE image. From the BSE image (Fig. 9a), it can observe that the Ag nanoparticles uniformly distributed on the Al-doped ZnO nanowires. Due to Ag and Sn have similar atomic numbers, which induced that only BSE images of larger Ag nanoparticles were more evident on the Al-doped ZnO@SnO_2 heteronanowires. Also, the TEM, HRTEM, and EDS mapping images (Fig. S12) of an Al-doped ZnO@SnO_2@Ag heterostructure (24 mM SnO_2 precursor) can use to confirm the hierarchical nanostructure, in which the Zn, Sn, and Ag signals exhibit similar shapes. This result indicated that an Al-doped ZnO@SnO_2@Ag heterostructure has been successfully fabricated in the reaction process.

To evaluate the importance of Ag nanoparticles on the Al-doped ZnO@SnO_2 heteronanowires, a high SERS response of the Raman-labeled molecules achieved. Herein, the influence of the different sizes of Al-doped ZnO@SnO_2 heteronanowires under the different concentration of SnO_2 reaction precursor on Raman intensity of R6G (10^{-6} M) systematically investigated, as shown in Fig. 10. The medium-strong and robust Raman bands were at the vibrational modes of R6G from the vibration of C—H stretching (1185 cm^{-1}), the N—H in-plane bend (1311 cm^{-1} and 1575 cm^{-1}) peaks, and C—C stretching (1361, 1510, and 1645 cm^{-1}) [75]. As the concentration of SnO_2 reaction precursor gradually increased from 12 to 48 mM, the intensity of the Raman signal at 1645 cm^{-1} exhibited a gradual decline. This phenomenon attributed to the growth of Al-doped ZnO@SnO_2 heteronanowires under the high concentration of SnO_2 reaction precursor, which exhibited larger sizes to reduce the number of hot spots in the three-dimensional structures, resulting the reduction of SERS intensity. Al-doped ZnO@SnO_2 heteronanowires (6 mM) can provide to deposit Ag nanoparticles with higher density and more hot spots in three-

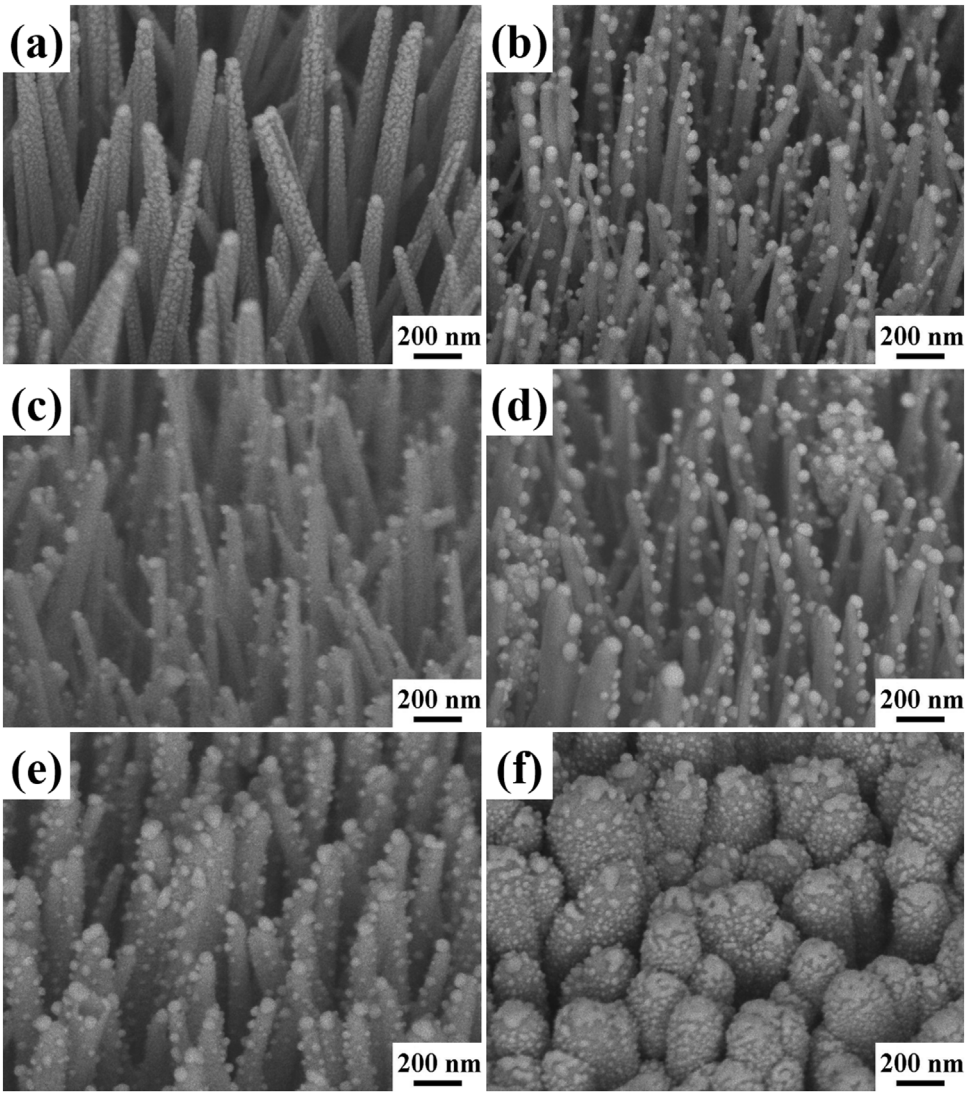

Fig. 9. The 45° tile-view backscatter electron (BSE) images of (a) Al-doped ZnO nanowires and (b–f) different sizes of Al-doped ZnO@SnO_2 heteronanowires fabricated on the glass substrates with the deposition of Ag nanoparticles. The different sizes of Al-doped ZnO@SnO_2 heteronanowires grown with the different concentrations of SnO_2 reaction precursor were (b) 3, (c) 6, (d) 12, (e) 24, and (f) 48 mM, respectively.

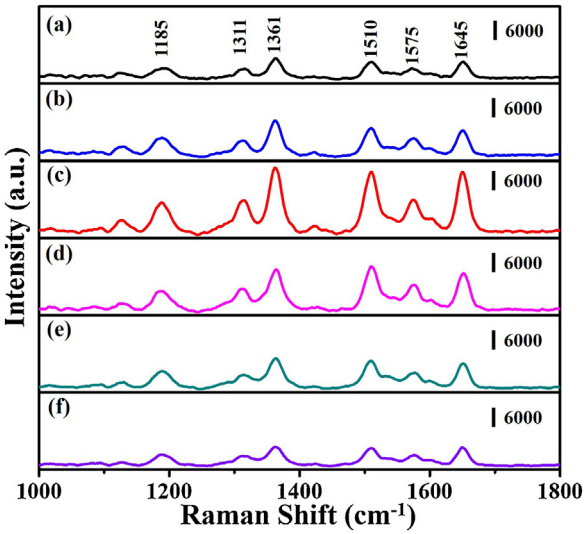

Fig. 10. The SERS spectra of R6G solution (1×10^{-6} M) collected on the (a) Al-doped ZnO nanowires (Fig. 1b) and (b–f) different sizes of Al-doped ZnO@SnO_2 heteronanowires (Fig. 1c–g) with Ag nanoparticle. The different sizes of Al-doped ZnO@SnO_2 heteronanowires grown with the different concentrations of SnO_2 reaction precursor were (b) 3, (c) 6, (d) 12, (e) 24, and (f) 48 mM, respectively.

dimensional structures, which were optimized to yield the greatest SERS effect.

In order to explore the uniformity of Al-doped ZnO@SnO_2@Ag heteronanowires (6 mM SnO_2 precursor) for SERS detection, we measured the SERS spectra of R6G from 10 random positions on the same Al-doped ZnO@SnO_2@Ag heteronanowires, as shown in Fig. 11a. There was no significant change in the position and intensity of the Raman peak, and all the intensity of the peaks were within 8% of the 10 points. This result revealed that the Al-doped ZnO@SnO_2@Ag heteronanowires have a highly uniform SERS enhancement effect. The reusability of SERS substrates was one of the fundamental and essential parameters of SERS applications. In the present study, the reusability (Fig. 11b) of the Ag nanoparticles decorated on the Al-doped ZnO@SnO_2 heteronanowires (6 mM SnO_2 precursor) can obtain from the same substrate for five cycles. For each cycle, this substrate was entirely regenerated by irradiated with 32 W UV lamp (Philip, λ_{max} = 254 nm) for 1 h. This substrate then immersed in the same concentration of R6G solution for another SERS cycle. This result implied that Ag nanoparticles decorated on the Al-doped ZnO@SnO_2 heteronanowires (6 mM SnO_2 precursor) can maintain similar SERS-enhancing effect even after five cycles. The SERS spectra (Fig. 12a) of R6G solution deposited on the Al-doped ZnO@SnO_2@Ag heteronanowires with various concentrations from 10^{-8} to 10^{-12} M. The intensity of the

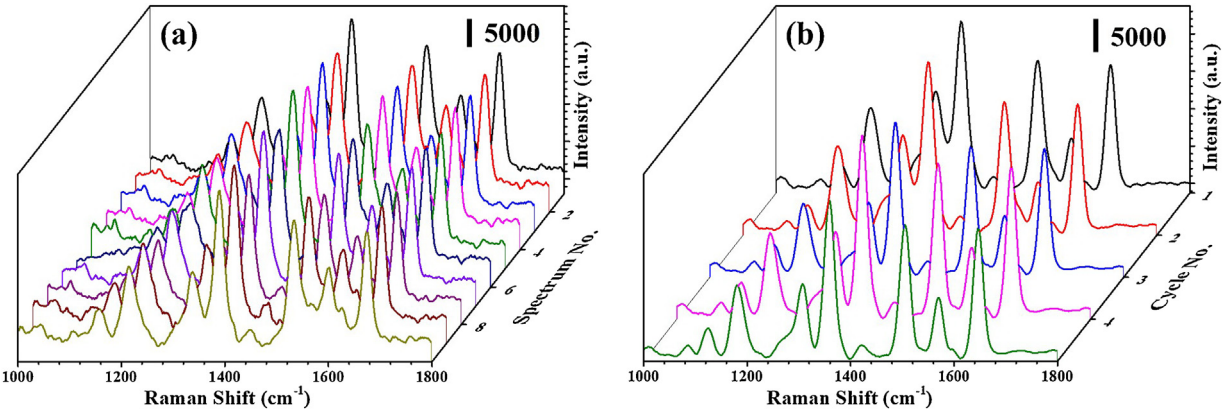

Fig. 11. (a) The SERS spectra of the R6 G solution (10^{-6} M) from 10 randomly selected spots on the Al-doped ZnO@SnO_2@Ag heteronanowires (6 mM SnO_2 precursor). (b) The reproducibility of the SERS spectra of R6 G (10^{-6} M) collected on the Al-doped ZnO@SnO_2@Ag heteronanowires (6 mM SnO_2 precursor).

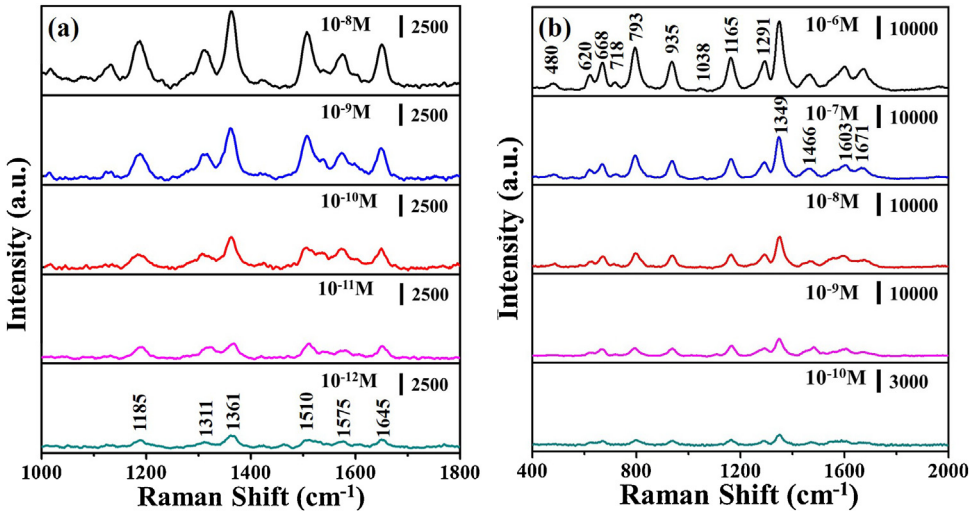

Fig. 12. (a) SERS spectra of different concentrations of R6G solution collected on the Al-doped ZnO@SnO_2@Ag heteronanowires (6 mM SnO_2 precursor). The concentrations of R6G solution were 10^{-8}, 10^{-9}, 10^{-10}, 10^{-11}, and 10^{-12} M, respectively. (b) SERS spectra of different concentrations of amoxicillin solution collected on the Al-doped ZnO@SnO_2@Ag heteronanowires (6 mM SnO_2 precursor). The concentrations of amoxicillin solution were 10^{-6}, 10^{-7}, 10^{-8}, 10^{-9}, and 10^{-10} M, respectively.

overall SERS peaks of R6G gradually decreased as the concentration of R6G decreased. Furthermore, the results also show that the SERS spectrum of the R6G solution can identify even at a concentration of 10^{-12} M.

To demonstrate that Al-doped ZnO@SnO_2@Ag heteronanowires can also use for drug detection. Here, we explored the SERS properties of Al-doped ZnO@SnO_2@Ag heteronanowires (6 mM SnO_2 precursor) by using amoxicillin as a probe molecule. Amoxicillin was an antibacterial drug that has been extensively used to treat bacterial infections in humans and animals [76]. The medium-strong and robust Raman bands of amoxicillin were 480 (ring deformation in thiazole), 620 (bending in O—H), 668 (ring deformation in benzene), 718 (stretching in C—C), 793 (in-plane deformation in C—H), 935 (bending in NH_2), 1038 (stretching in NH_2 and C—H), 1165 (C—H bending in benzene ring), 1291 (in-plane deformation in benzene), 1349 (twisting in NH_2), 1466 (asymmetric bending in CH_3), 1603 (stretching in benzene ring), and 1671 cm^{-1} (bending in N—H), respectively [77,78]. Fig. 12b shows the SERS spectra of amoxicillin solution deposited on the Al-doped ZnO@SnO_2@Ag heteronanowires with various concentrations from 10^{-6} to 10^{-10} M. The intensity of the overall SERS peaks of amoxicillin gradually decreased as the concentration of amoxicillin declined. Furthermore, the results also show that the SERS spectrum of the amoxicillin solution can identify even at a concentration of 10^{-10} M. Herein, the detection concentration of amoxicillin can be as lower as 10^{-10} M, which was lower than the value of the previous report detection concentration (10^{-8} M) [77]. The results indicated that Al-doped ZnO@SnO_2@Ag heteronanowires may be suitable for trace detection of organic pollutants and drugs.

Conclusion

The bi-functional Al-doped ZnO@SnO_2 heteronanowires can directly grow on the glass substrates via the combination of wet chemical and hydrothermal methods. The effects of the concentration of SnO_2 precursor and reaction time for the morphology, crystal structures, optical absorption, and emission properties, photocatalytic efficiency and stability of Al-doped ZnO@SnO_2 heteronanowires explored. Compared to Al-doped ZnO nanowires, Al-doped ZnO@SnO_2 heteronanowires can provide efficient electron–hole pairs separation and high surface active sites for improving the photodecomposition of R6G solution under low-powered UV-light irradiation. Also, Al-doped ZnO@SnO_2 heteronanowires revealed better photodegradation efficiency than commercial ZnO or TiO_2 nanopowder. Moreover, appropriate shell-thicknesses of Al-doped ZnO@SnO_2 heteronanowires exhibited suitable geometry to deposit Ag nanoparticles with higher density and more hot spots in three-dimensional structures for improving SERS efficiency in the detection of R6G molecule. Al-doped ZnO@SnO_2@Ag heteronanowires can not only provide high enhancement, high reproducibility, and the low detection limit for the SERS detection of R6G molecule but also use for SERS detection of amoxicillin molecule with low detection limit.

Acknowledgments

This work is financially supported by the Ministry of Science and Technology, Taiwan (MOST 106-2221-E-035-032-MY3 and MOST 107-2218-E-035-010-). The authors appreciate the Precision Instrument Support Center of Feng Chia University in providing the fabrication and measurement facilities.

Appendix A. Supplementary data

Supplementary material related to this article can be found, in the online version, at doi:https://doi.org/10.1016/j.jiec.2019.03.058.

References

[1] N. Tripathy, R. Ahmad, J. Eun Song, H. Ah Ko, Y.-B. Hahn, G. Khang, Mater. Lett. 136 (2014) 171.
[2] F. Han, V.S.R. Kambala, M. Srinivasan, D. Rajarathnam, R. Naidu, Appl. Catal. A 359 (2009) 25.
[3] F.-H. Ko, W.-J. Lo, Y.-C. Chang, J.-Y. Guo, C.-M. Chen, J. Alloys Compd. 678 (2016) 137.
[4] D.S. Bhatkhande, V.G. Pangarkar, A.A.C.M. Beenackers, J. Chem. Technol. Biotechnol. 77 (2002) 102.
[5] A. Houas, H. Lachheb, M. Ksibi, E. Elaloui, C. Guillard, J.-M. Herrmann, Appl. Catal. B 31 (2001) 145.
[6] H. Gao, H. Yang, J. Xu, S. Zhang, J. Li, Small 14 (2018)1801353.
[7] P.-Y. Hsieh, Y.-H. Chiu, T.-H. Lai, M.-J. Fang, Y.-T. Wang, Y.-J. Hsu, ACS Appl. Mater. Interfaces 11 (2019) 3006.
[8] S. Zhang, H. Gao, Y. Huang, X. Wang, T. Hayat, J. Li, X. Xu, X. Wang, Environ. Sci. Nano 5 (2018) 1179.
[9] H. Gao, R. Cao, X. Xu, S. Zhang, H. Yongshun, H. Yang, X. Deng, J. Li, Appl. Catal. B 245 (2019) 399.
[10] S. Adhikari, D. Sarkar, G. Madras, RSC Adv. 5 (2015) 11895.
[11] M. Ge, C. Cao, J. Huang, S. Li, Z. Chen, K.-Q. Zhang, S.S. Al-Deyab, Y. Lai, J. Mater. Chem. A 4 (2016) 6772.
[12] K. Nakata, A. Fujishima, J. Photochem. Photobiol. C 13 (2012) 169.
[13] R. Tong, X. Wang, X. Zhou, Q. Liu, H. Wang, X. Peng, X. Liu, Z. Zhang, H. Wang, P. D. Lund, Int. J. Hydrogen Energy 42 (2017) 5496.
[14] C. He, X. Peng, Q. Liu, X. Fan, H. Wang, Int. J. Hydrogen Energy 39 (2014) 13415.
[15] S.G. Kumar, K.S.R.K. Rao, RSC Adv. 5 (2015) 3306.
[16] K. Wetchakun, N. Wetchakun, S. Sakulsermsuk, J. Ind. Eng. Chem. 71 (2019) 19.
[17] B. Krishnakumar, T. Imae, Appl. Catal. A 486 (2014) 170.
[18] C.-M. Chou, Y.-C. Chang, P.-S. Lin, F.-K. Liu, Mater. Chem. Phys. 201 (2017) 18.
[19] X. Zhang, J. Qin, Y. Xue, P. Yu, B. Zhang, L. Wang, R. Liu, Sci. Rep. 4 (2014) 4596.
[20] L. Zhang, H. Yang, J. Ma, L. Li, X. Wang, L. Zhang, S. Tian, X. Wang, Appl. Phys. A 100 (2010) 1061.
[21] Z. Yu, H. Moussa, Y. Ma, M. Liu, B. Chouchene, R. Schneider, M. Moliere, H. Liao, J. Colloid Interface Sci. 534 (2019) 637.
[22] Y.-C. Chang, P.-S. Lin, F.-K. Liu, J.-Y. Guo, C.-M. Chen, J. Alloys Compd. 688 (2016) 242.
[23] L. Pan, T. Muhammad, L. Ma, Z.-F. Huang, S. Wang, L. Wang, J.-J. Zou, X. Zhang, Appl. Catal. B 189 (2016) 181.
[24] H.-M. Chiu, T.-H. Yang, Y.-C. Hsueh, T.-P. Perng, J.-M. Wu, Appl. Catal. B 163 (2015) 156.
[25] Q. Wang, B. Geng, S. Wang, Environ. Sci. Technol. 43 (2009) 8968.
[26] V. Vaiano, M. Matarangolo, J.J. Murcia, H. Rojas, J.A. Navío, M.C. Hidalgo, Appl. Catal. B 225 (2018) 197.
[27] P. She, K. Xu, S. Yin, Y. Shang, Q. He, S. Zeng, H. Sun, Z. Liu, J. Colloid Interface Sci. 514 (2018) 40.
[28] H. Wang, X. Qiu, W. Liu, D. Yang, Appl. Surf. Sci. 426 (2017) 206.
[29] A. Shirzadi, A. Nezamzadeh-Ejhieh, J. Mol. Catal. A: Chem. 411 (2016) 222.
[30] B. Krishnakumar, A. Balakrishna, S.A. Nawabjan, V. Pandiyan, A. Aguiar, A.J.F.N. Sobral, J. Phys. Chem. Solids 111 (2017) 364.
[31] B. Krishnakumar, T. Imae, J. Miras, J. Esquena, Sep. Purif. Technol. 132 (2014) 281.
[32] X. Zhou, X. Wang, R. Tong, L. Xiao, Z. Zheng, X. Peng, H. Wang, H. Wang, Int. J. Energ. Res. 41 (2017) 1781.
[33] X. Zheng, D. Li, X. Li, J. Chen, C. Cao, J. Fang, J. Wang, Y. He, Y. Zheng, Appl. Catal. B 168–169 (2015) 408.
[34] Y.-C. Chang, J. Alloys Compd. 664 (2016) 538.
[35] S.V.P. Vattikuti, P.A.K. Reddy, J. Shim, C. Byon, ACS Omega 3 (2018) 7587.
[36] S. Balachandran, M. Swaminathan, Dalton Trans. 42 (2013) 5338.
[37] Y.-C. Chang, J.-Y. Guo, C.-M. Chen, H.-W. Di, C.-C. Hsu, Nanoscale 9 (2017) 13235.
[38] C. Xu, J. Sun, L. Gao, J. Mater. Chem. 22 (2012) 975.
[39] V. Velmurugan, U. Srinivasarao, R. Ramachandran, M. Saranya, A.N. Grace, Mater. Res. Bull. 84 (2016) 145.
[40] S. Wang, W. Yu, C. Cheng, T. Zhang, M. Ge, Y. Sun, N. Dai, Mater. Res. Bull. 89 (2017) 267.
[41] H.-Y. Chen, D.-B. Kuang, C.-Y. Su, J. Mater. Chem. 22 (2012) 15475.
[42] Y.-C. Chang, J.-C. Lin, S.-Y. Chen, L.-Y. Hung, Y.-R. Lin, C.-Y. Chen, Mater. Res. Bull. 100 (2018) 429.
[43] L. Zhu, M. Hong, G. Wei Ho, Sci. Rep. 5 (2015) 11609.
[44] Z. Zhang, C. Shao, X. Li, L. Zhang, H. Xue, C. Wang, Y. Liu, J. Phys. Chem. C 114 (2010) 7920.
[45] C.-C. Lin, Y.-J. Chiang, Chem. Eng. J. 181–182 (2012) 196.
[46] R. Lamba, A. Umar, S.K. Mehta, S. Kumar Kansal, Talanta 131 (2015) 490.
[47] N.T. Khoa, S.W. Kim, D.-H. Yoo, S. Cho, E.J. Kim, S.H. Hahn, ACS Appl. Mater. Interfaces 7 (2015) 3524.
[48] J. Wang, N. Du, H. Zhang, J. Yu, D. Yang, J. Phys. Chem. C 115 (2011) 11302.
[49] S. Cong, Y. Yuan, Z. Chen, J. Hou, M. Yang, Y. Su, Y. Zhang, L. Li, Q. Li, F. Geng, Z. Zhao, Nat. Commun. 6 (2015) 7800.
[50] G.A. Baker, D.S. Moore, Anal. Bioanal. Chem. 382 (2005) 1751.
[51] W.H. Do, C.J. Lee, D.Y. Kim, M.J. Jung, J. Ind. Eng. Chem. 18 (2012) 2141.
[52] H. Jun Yin, Z. Yang Chen, Y. Mei Zhao, M. Yang Lv, C. An Shi, Z. Long Wu, X. Zhang, L. Liu, M. Li Wang, H. Jun Xu, Sci. Rep. 5 (2015) 14502.
[53] C. Novara, S. Dalla Marta, A. Virga, A. Lamberti, A. Angelini, A. Chiadò, P. Rivolo, F. Geobaldo, V. Sergo, A. Bonifacio, F. Giorgis, J. Phys. Chem. C 120 (2016) 16946.

[54] W.-H. Park, Z.H. Kim, Nano Lett. 10 (2010) 4040.
[55] Y. Li, J. Dykes, T. Gilliam, N. Chopra, Nanoscale 9 (2017) 5263.
[56] L.A. Lane, X. Qian, S. Nie, Chem. Rev. 115 (2015) 10489.
[57] R. Gunawidjaja, E. Kharlampieva, I. Choi, V.V. Tsukruk, Small 5 (2009) 2460.
[58] Y. Li, W. Shi, A. Gupta, N. Chopra, RSC Adv. 5 (2015) 49708.
[59] Y.-C. Chang, Sens. Actuators B: Chem. 225 (2016) 498.
[60] H. Tang, G. Meng, Q. Huang, Z. Zhang, Z. Huang, C. Zhu, Adv. Funct. Mater. 22 (2012) 218.
[61] J. Huang, F. Chen, Q. Zhang, Y. Zhan, D. Ma, K. Xu, Y. Zhao, ACS Appl. Mater. Interfaces 7 (2015) 5725.
[62] Y.-C. Chang, C.-C. Hsu, S.-H. Wu, K.-W. Chuang, Y.-F. Chen, Appl. Surf. Sci. 447 (2018) 213.
[63] C.-M. Chou, Y.-C. Chang, P.-S. Lin, F.-K. Liu, J. Photochem. Photobiol. A: Chem. 347 (2017) 1.
[64] Q. Cao, X. Liu, K. Yuan, J. Yu, Q. Liu, J.-J. Delaunay, R. Che, Appl. Catal. B 201 (2017) 607.
[65] J. Mass, P. Bhattacharya, R.S. Katiyar, Mater. Sci. Eng. B 103 (2003) 9.
[66] V. Gaddam, R.R. Kumar, M. Parmar, G.R.K. Yaddanapudi, M.M. Nayak, K. Rajanna, RSC Adv. 5 (2015) 13519.
[67] S. Bai, T. Guo, Y. Zhao, R. Luo, D. Li, A. Chen, C.C. Liu, J. Mater. Chem. A 1 (2013) 11335.
[68] A. Kar, S. Sain, D. Rossouw, B.R. Knappett, S.K. Pradhan, G.A. Botton, A.E.H. Wheatley, J. Alloys Compd. 698 (2017) 944.
[69] R. Wei, K. Du, X. Gong, Q. Chen, Z. Tang, J. You, L. Li, H. Yang, Appl. Surf. Sci. 255 (2009) 6464.
[70] R. Yogamalar, V. Mahendran, R. Srinivasan, A. Beitollahi, R.P. Kumar, A.C. Bose, A. Vinu, Chem. Asian J. 5 (2010) 2379.
[71] J. Li, S. Meng, T. Wang, Q. Xu, L. Shao, D. Jiang, M. Chen, Appl. Surf. Sci. 396 (2017) 430.
[72] B. Babu, I. Neelakanta Reddy, K. Yoo, D. Kim, J. Shim, Mater. Lett. 221 (2018) 211.
[73] A.N. Kadam, D.P. Bhopate, V.V. Kondalkar, S.M. Majhi, C.D. Bathula, A.-V. Tran, S.-W. Lee, J. Ind. Eng. Chem. 61 (2018) 78.
[74] C. Jia, H.-S. Chen, P. Yang, J. Ind. Eng. Chem. 58 (2018) 278.
[75] D. Pristinski, S. Tan, M. Erol, H. Du, S. Sukhishvili, J. Raman Spectrosc. 37 (2006) 762.
[76] T.-H. Chang, Y.-C. Chang, C.-M. Chen, K.-W. Chuang, C.-M. Chou, J. Alloys Compd. 782 (2019) 887.
[77] G. Kibar, A.E. Topal, A. Dana, A. Tuncel, J. Mol. Struct. 1119 (2016) 133.
[78] A. Bebu, L. Szabó, N. Leopold, C. Berindean, L. David, J. Mol. Struct. 993 (2011) 52.